




Quantum description of atomic diffraction by material nanostructures

Charles Garcion,^{1,2} Quentin Bouton ,¹ Julien Lecoffre,¹ Nathalie Fabre ,¹ Éric Charron ,³ Gabriel Dutier,¹ and Naceur Gaaloul²

¹Laboratoire de Physique des Lasers, Université Sorbonne Paris Nord, CNRS UMR 7538, F-93430, Villetaneuse, France

²Leibniz University of Hanover, Institute of Quantum Optics, QUEST-Leibniz Research School, Hanover, Germany

³Université Paris-Saclay, CNRS, Institut des Sciences Moléculaires d'Orsay, F-91405 Orsay, France



(Received 12 December 2023; accepted 1 April 2024; published 13 May 2024)

We present a theoretical model of matter-wave diffraction through a material nanostructure. This model is based on the numerical solution of the time-dependent Schrödinger equation, which goes beyond the standard semiclassical approach. In particular, we consider the dispersion force interaction between the atoms and the material, which is responsible for high energy variations. The effect of such forces on the quantum model is investigated, along with a comparison with the semiclassical model. In particular, for atoms at low velocity and close to the material surface, the semiclassical approach fails, while the quantum model accurately describes the expected diffraction pattern. This description is thus relevant for slow and cold atom experiments where increased precision is required, e.g., for metrological applications.

DOI: [10.1103/PhysRevResearch.6.023165](https://doi.org/10.1103/PhysRevResearch.6.023165)

I. INTRODUCTION

Atomic interferometry using light pulses [1], magnetic gradients [2], and material gratings [3] is now a mature field of physics. In particular, advances in the cooling and control of atoms have turned this field into a versatile tool for precise measurements with applications in fundamental physics tests [4] or accurate inertial sensing [5]. In this paper, we focus on atomic diffraction patterns formed by material gratings where dispersion forces such as Casimir-Polder play an important role. These forces between the particle and the grating walls are created by the ground-state fluctuations of the electromagnetic fields, generally resulting in an attractive potential [6]. They are of far-reaching importance in chemistry, biology, cosmology, atomic force microscopy [7] and can be used as a test of quantum electrodynamics. Interest in understanding this interaction also stems from its application, e.g., in the development of atomic lithography [8]. The role of this interaction is all the more important since the mechanical gratings used in atomic interferometry experiments are usually built on the nanometer scale. Using nanofabricated transmission gratings (called nanograting), the influence of this force has been studied for alkali atoms [9,10], excited noble gases [11,12], or even complex molecules [13]. Furthermore, this approach has recently allowed to distinguish between the nonretarded and the retarded regime of the Casimir-Polder interaction in the intermediate range [14]. Such interferometers can also be configured to measure, for example, atomic polarizability with high sensitivity [15], dynamic polarizability of large molecules [16], and inertial signals [17].

These matter-wave experiments require quantitative simulations to bridge the gap between theory and experiment. The current theoretical framework used so far to account for the dispersion forces is based on a semiclassical approach in the eikonal approximation [18] and beyond [19]. This method remains valid if the action S over the classical trajectories through the interaction region is much larger than \hbar , if the de Broglie wavelength λ of the particle is much shorter than the spatial variation of the interaction potential V , and if the spatial variation of the de Broglie wavelength is small. These approximations fail in close vicinity of the walls, where the dispersion force is dominant, and for low atom velocities. In both cases, the interaction potential exceeds the kinetic energy. Triggered by (i) the increased precision required in metrology, (ii) the need to probe the dispersion forces close to the surface, and (iii) the experimental progress in cooling and slowing atoms to increase the interaction time between the atoms and the nanograting thus enhancing the sensitivity of the measurements [14], it becomes necessary to advance the theoretical description of material matter-wave interference beyond the semiclassical approach.

We present here a matter-wave diffraction model based on a numerically efficient solution of the time-dependent Schrödinger equation. Owing to the fast developments in the field of matter-wave optics in the last decade, numerical simulations involving atom-surface interactions have been developed in the context of quantum reflection [20,21]. Here, by exploring short atom-surface distances where large energy variations occur, we reproduce matter-wave diffraction patterns beyond the semiclassical approach.

The structure of the paper is as follows: In Sec. II, we describe the theoretical approach, introducing the dispersion forces used and the approximation adopted in the immediate vicinity of the surface. Section III is devoted to the numerical performance and to the description of the diffraction pattern in the far-field regime. In Sec. IV, the numerical results

Published by the American Physical Society under the terms of the [Creative Commons Attribution 4.0 International](https://creativecommons.org/licenses/by/4.0/) license. Further distribution of this work must maintain attribution to the author(s) and the published article's title, journal citation, and DOI.

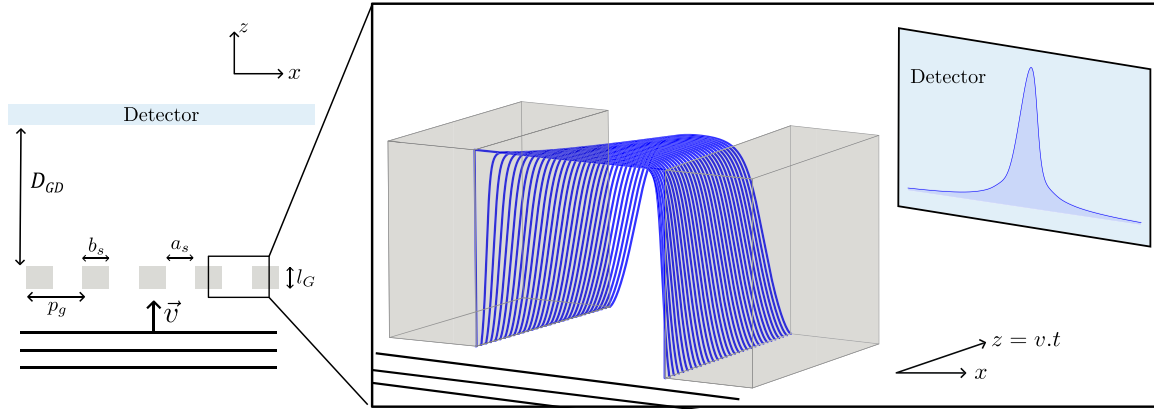


FIG. 1. On the left, a schematic illustration of the problem considered. A plane wave representing a single particle with velocity v hits a N -slit nanograting. The detection takes place at a distance D_{GD} from the slits. The nanograting has the following geometry: slit size a_s , wall slit b_s , thickness l_G , and periodicity $p_g = a_s + b_s$. On the right is the result of a typical time evolution of the wave function inside the slits, with $a_s = 100$ nm, $b_s = 100$ nm, and $l_G = 100$ nm, which are typical dimensions used in experiments. In the back plane a characteristic one-slit wave function is plotted after free propagation to the detector. This function is the envelope of the N -slit wave function.

obtained are compared with the semiclassical approach. Finally, summary and conclusion are given in Sec. V.

II. THEORETICAL MODEL

A. Representation of the problem

In this section we outline the matter-wave interference pattern from a N -slits nanograting in the far-field limit and show that the problem can be reduced to a single-slit problem. The system studied is illustrated schematically in Fig. 1. The coordinate system is chosen such that the grating lies in the (xy) plane and z is the propagation direction. The incoming atoms, of mass m , are described by an incident plane wave $\psi_{\text{inc}}(z) = \exp(ikz)$ with $k = 2\pi/\lambda$, where λ is the de Broglie wavelength of the atoms [22]. This incident plane wave interacts with a N -slits nanograting of slit size $a_s = 100$ nm, wall width $b_s = 100$ nm and thickness $l_G = 100$ nm (see Fig. 1). We also assume that the slits are large enough along the z axis to ignore the diffraction pattern along this given direction. The grating periodicity $p_g = a_s + b_s$ implies that the total wave function inside the grating can be expressed as the given quantum superposition

$$\psi(x, t) = \sum_{n=0}^{N-1} \psi_n(x, t), \quad (1)$$

where $\psi_n(x, t)$ represents the wave function of the particle inside the n th slit. We also assume that the slits are independent and identical, allowing us to write $\psi_n(x, t) = \psi_0(x - np_g, t)$. After an interaction time $t_e = l_G/v$ inside the grating, where $v = \hbar k/m$ is the particle velocity, the Fourier transform of the total wave function at the exit of the grating is simply given by

$$\tilde{\psi}(k, t_e) = \tilde{\psi}_0(k, t_e) \left[\frac{\sin\left(\frac{Nkp_g}{2}\right)}{\sin\left(\frac{kp_g}{2}\right)} \right] e^{i\frac{(N-1)}{2}kp_g}. \quad (2)$$

Thereafter, the atoms freely evolve to the detector during a time T , leading to the following expression of the propagated

wave function in the Fourier domain

$$\tilde{\psi}(k, t_e + T) = \tilde{\psi}(k, t_e) e^{-i\frac{\hbar k^2}{2m}T}. \quad (3)$$

Many nanograting experiments take place in the far-field regime, i.e., after a long propagation time. In this model, the diffraction signal is therefore computed using the stationary phase approximation (see Appendix A and e.g., Ref. [23]). Following this assumption, the wave function in coordinate space and at the detector position can be expressed as

$$\psi(x, t_e + T) \simeq \sqrt{\frac{m}{\hbar T}} \tilde{\psi}\left(\frac{mx}{\hbar T}, t_e\right) e^{i\frac{mx^2}{2\hbar T}} e^{-i\frac{\pi}{4}}. \quad (4)$$

In the typical cases that we are going to encounter in this study, this approximation yields negligible error, the error bound with the second-order correction being below 2×10^{-4} (see Appendix A). It also avoids scaling problems in terms of number of grid points required to numerically compute the far-field diffraction pattern. Finally, under this approximation the final probability density can be simply expressed as

$$|\psi(x, t_e + T)|^2 \simeq \frac{m}{\hbar T} \left[\frac{\sin(Nk_g x)}{\sin(k_g x)} \right]^2 |\tilde{\psi}_0(k_s, t_e)|^2 \quad (5)$$

where

$$k_g = \frac{mp_g}{2\hbar T}. \quad (6)$$

In this expression, $|\tilde{\psi}_0(k_s, t_e)|^2$ is the atomic probability density diffracted by a single slit. In the limit of large slit numbers ($N \gg 1$), this expression can be further simplified to

$$|\psi(x, t_e + T)|^2 \propto |\tilde{\psi}_0(k_s, t_e)|^2 \sum_i \delta\left(x - i\frac{\lambda D_{GD}}{p_g}\right), \quad (7)$$

where $\delta(x)$ is the Dirac delta function and D_{GD} the grating-detector distance. As a result, the problem in the far-field regime, where the wave pattern is expanded well beyond the size of the slit a_s , is reduced to simulating the propagation through a single slit.

B. Potential inside the slits

The existence of forces between the atoms and the slit surface is due to the Casimir-Polder interaction [24,25]. In this article, we consider the dispersion force inside the slits for atoms in the vicinity of a surface, neglecting the retardation effects resulting from the finite-field propagation time between the atoms and the surface. In major nonresonant atom-surfaces cases, such effects become significant at distances larger than $\lambda_{\text{opt}}/(2\pi)$, where λ_{opt} represents the optical transition wavelengths of the species. However, in this study, the maximum atom-surface distance considered ($a_s/2 = 50$ nm) is generally smaller, resulting in little retardation effects (around 10% of the total potential contribution). In this simplified case, the potential, also called the nonretarded Casimir-Polder or van der Waals interaction, is written for the two walls of the slits located at $x = \pm a_s/2$ as

$$V_{vdW}(x) = -\frac{C_3}{(a_s/2 - x)^3} - \frac{C_3}{(a_s/2 + x)^3}, \quad (8)$$

where C_3 is a coefficient describing the strength of the interaction. This coefficient depends on the polarizability of the atom and on the dielectric response of the wall material. Inspired by the experimental setup reported in [14], we consider argon atoms in the 3P_2 state interacting with a Si_3N_4 grating, giving $C_3 = 5.04$ meV nm³ [26]. This number is within the usual range of values observed in the majority of atomic diffraction experiments due to similarity in nanograting materials and comparable atomic polarizabilities [3]. Furthermore, $\lambda_{\text{opt}} = 811$ nm (for Ar in its 3P_2 state) ensures that retardation effects are negligible for the atom-surface distances examined in this study. When the wave functions of the atoms start to overlap with the electrons of the surface, an additional short-range repulsive contribution arises due to the Pauli repulsion. We model such a contribution with the repulsive part of a 9-3 Lennard-Jones potential for each wall of the slit [27,28]

$$V_{LJ}(x) = \frac{C_{\text{rep}}}{(a_s/2 - x)^9} + \frac{C_{\text{rep}}}{(a_s/2 + x)^9}, \quad (9)$$

where C_{rep} is a strength coefficient. Such potential scaling arises from the pairwise Lennard-Jones interaction in $1/x^{12}$ with the atoms of the surface (see Appendix C). The total potential is thus $V_{TOT}(x) = V_{vdW}(x) + V_{LJ}(x)$ and is represented in Fig. 2(a). In the following, we fix the position of the minimum potential at a distance r_{min} from the walls. This implies that the coefficients C_3 , r_{min} and C_{rep} are no longer independent and are related by $3C_{\text{rep}} = C_3 r_{\text{min}}^6$. For the simulation, we use $r_{\text{min}} = 0.35$ nm, which corresponds to the radius of 3P_2 argon atoms in a solid sphere model (see Appendix B).

C. Adjustment of the potential and wave function absorption

As seen in Fig. 2(a), the overlapping between the wave functions of the atoms and the surface occurs for atom-surface distances shorter than r_{min} , leading to sticking processes [29] or internal state transfer [30] for the atoms. In all cases, such atoms are lost and do not contribute to the diffraction pattern signal. Wave function reflections for the short-range regime are thus annihilated, and an absorption method must

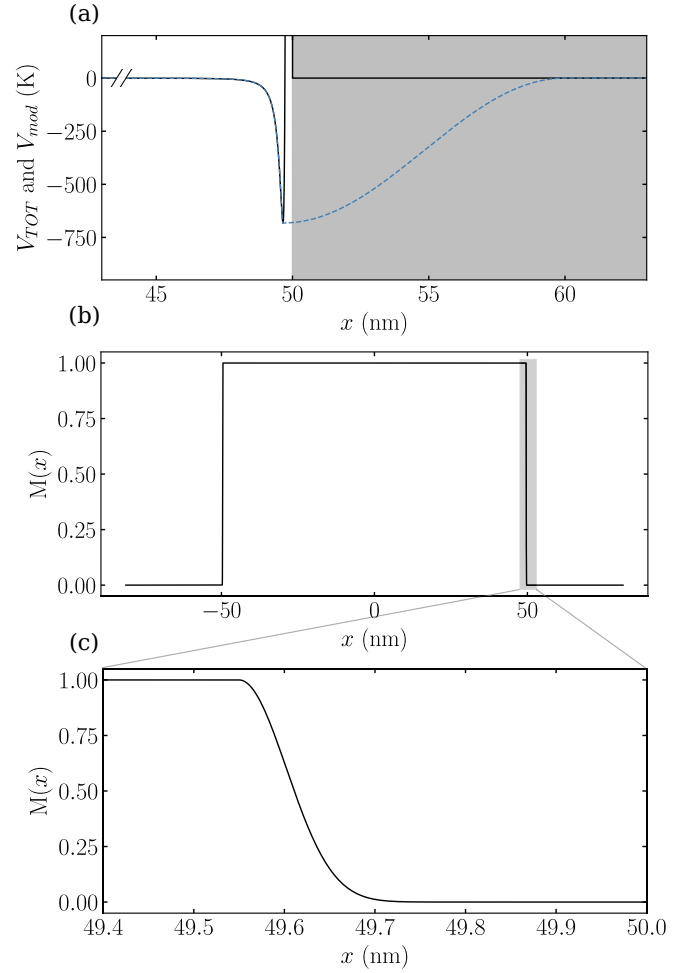


FIG. 2. (a) Total potential $V_{TOT}(x) = V_{vdW}(x) + V_{LJ}(x)$ (solid-black line) as a function of the distance x inside the slits. The grey area represents a wall located at $x = a_s/2 = 50$ nm. The blue dashed curve represents the modified potential $V_{mod}(x)$. (b) Mask function $M(x)$ used to absorb the wave function close to the surfaces. Here $d = 0.2$ nm and $x_{\text{abs}} = 49.75$ nm (c) Zoom on the mask function $M(x)$. The plots typically use parameters inspired by the experimental setup described in Ref. [14].

be implemented. Hence, an adjustment of the potential V_{TOT} is introduced in the model [20]. The underlying idea is to replace the repulsive part of the potential to improve the absorption effect. In the simulation we use the modified potential $V_{mod}(x)$ defined as follows. Inside the slit and far from the surfaces, i.e., for $|x| \leq a_s/2 - r_{\text{min}}$, $V_{mod}(x) = V_{TOT}(x)$. In the vicinity of the slit surface, i.e., for $a_s/2 - r_{\text{min}} \leq |x| \leq a_s/2 + l_{ab}$,

$$V_{mod}(x) = U_0 \cos^2 \left[\frac{\pi(|x| - a_s/2 + r_{\text{min}})}{2(l_{ab} + r_{\text{min}})} \right], \quad (10)$$

where $U_0 = V_{TOT}(a_s/2 - r_{\text{min}})$ is the minimum of the potential and l_{ab} is the distance over which the potential $V_{mod}(x)$ goes from U_0 to 0 (see Fig. 2). And finally, for $|x| \geq a_s/2 + l_{ab}$, $V_{mod}(x) = 0$. A typical value for l_{ab} in the simulation is $l_{ab} = 10$ nm. This modified potential, as well as its derivatives, are continuous at the positions $|x| = a_s/2 - r_{\text{min}}$.

To account for atomic losses near the boundaries $|x| = a_s/2 - r_{\text{min}}$, we introduce a mask function $M(x)$ to impose

absorbing boundary conditions. In practice, this is done in a simple way since the wave function $\psi(x, t)$ is multiplied by $M(x)$ after each time step of the propagation. This absorption technique is similar to other absorptions methods such as the imaginary negative potential [31] or the complex absorption potential [32]. The mask function has been tailored for our specific case. It is defined as follows. Inside the slit and far from the surfaces, i.e., for $|x| \leq x_{abs} - d$, $M(x) = 1$. Here x_{abs} is the position where the wave function is absorbed and d is half the total absorption length. In the absorption region, i.e., for $x_{abs} - d \leq |x| \leq x_{abs} + d$ we have

$$M(x) = \cos^{12} \left[\frac{\pi (|x| - x_{abs} + d)}{4d} \right]. \quad (11)$$

And for $|x| \geq x_{abs} + d$, $M(x) = 0$. The parameter x_{abs} is chosen so that the absorption occurs at a correct distance from the wall. For the simulations we use $d = 0.2$ nm and $x_{abs} = 49.75$ nm [see Fig. 2(b) and 2(c)]. Geometrical grating details along the depth can also be implemented in the model, such as opening angles of the slit widths [29], for example by considering a time-dependent slit size a_s . For simplicity, the slit size a_s is kept constant in the following. Finally, we choose the initial wave function at the entrance of the slit to be proportional to the mask function

III. NUMERICAL METHOD

The 1D time-dependent Schrödinger equation is solved numerically using the second-order split-operator technique [33]. For the simulations performed in this section, the initial atom velocity is set to $v = 20$ m/s and the nanograting geometry properties are $a_s = 100$ nm, $b_s = 100$ nm and $l_G = 100$ nm. The spatial grid resolution is $\delta x = 2.5$ pm and the time step is $\delta t = 0.25$ ps, values for which the simulations numerically converged. The number of grid points used is 2^{16} . The grating-detector distance is fixed at $D_{GD} = 300$ nm such as the detection takes place in the far-field regime with a Fresnel number $\mathcal{F} = a_s^2 / (\lambda D_{GD}) \ll 10^{-3}$.

A. Probability density inside the slit

Figure 3 shows the square modulus of the wave function at the exit of the slit $|\psi_0(x, t_e)|^2$. We observe that the probability of finding an atom near the surface is low. This is due to atom losses when hitting the surface during the propagation. We can also observe that the absorption of the wave function occurs over a length of about 0.1 nm, which is smaller than the absorption length $d = 0.2$ nm. We can also verify that the damped part of the wave function is centered around 49.65 nm, which corresponds to $r_{min} = 0.35$ nm.

The mask function and the associated absorbing length d affect the shape of the wave function $\psi_0(x, t)$ near the surface where the absorption occurs. Therefore, to quantify the influence of both the absorbing length d and the modified potential $V_{mod}(x)$ on the wave function $\psi(x, t)$, we introduce the ratio $r(t)$ between the integral of the square modulus of the wave function in the absorbing region, with the integral of

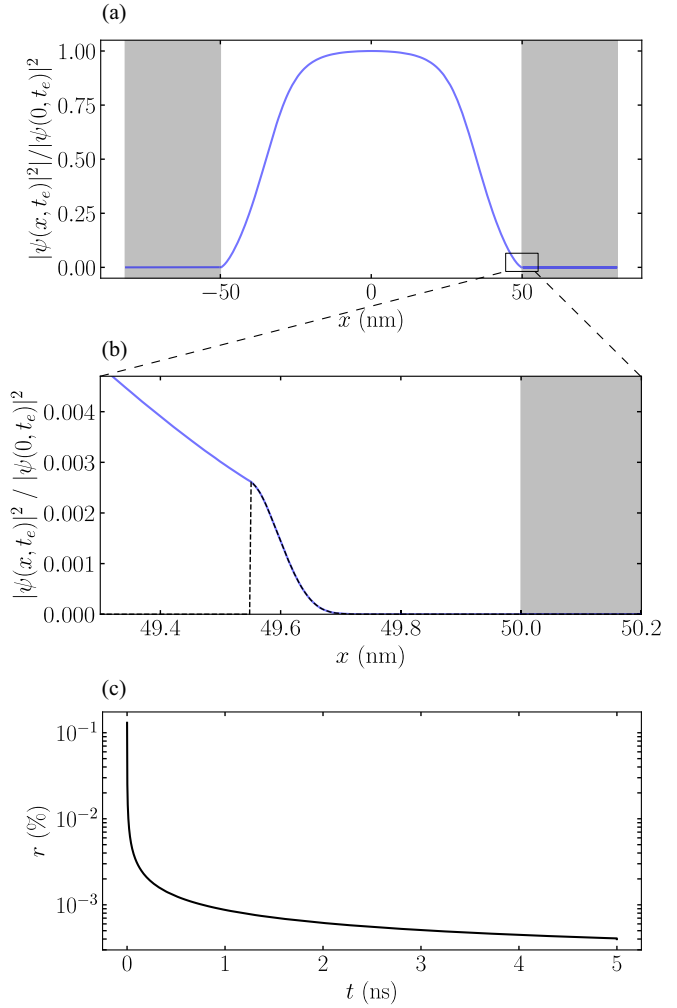


FIG. 3. (a) In the solid-blue line, the square modulus of the wave function $|\psi(x, t_e)|^2$ at the exit of the slit. The two grey areas represent the slit walls. In (b), zoom on $|\psi(x, t_e)|^2$ close to the surface. The black-dashed line indicates the modification area of the wave function due to the absorption region ($x \geq x_{abs} - d$). (c) Time evolution of the ratio $r(t)$ in a log scale. The graphs utilize parameters based on the experiment outlined in [14].

the square modulus of the total wave function

$$r(t) = \frac{2 \int_{x_{abs}-d}^{+\infty} |\psi_0(x, t)|^2 dx}{\int_{-\infty}^{+\infty} |\psi_0(x, t)|^2 dx}. \quad (12)$$

At the entrance of the slit (time $t = 0$) we have $r(0) \simeq 0.125\%$ and at the exit ($t = t_e$) we have $r(t_e) \simeq 4.1 \times 10^{-4}\%$. The decrease of $r(t)$ is explained by the reduction of the amplitude of the wave function near the walls due to atoms losses. The small initial value and rapid decrease of $r(t)$ [see Fig. 3(c)] justifies that the absorbing length d is sufficiently small to have a negligible influence on the wave function at the exit of the slit. Furthermore, it also supports the statement that the modification of the repulsive part of the potential has a minor impact.

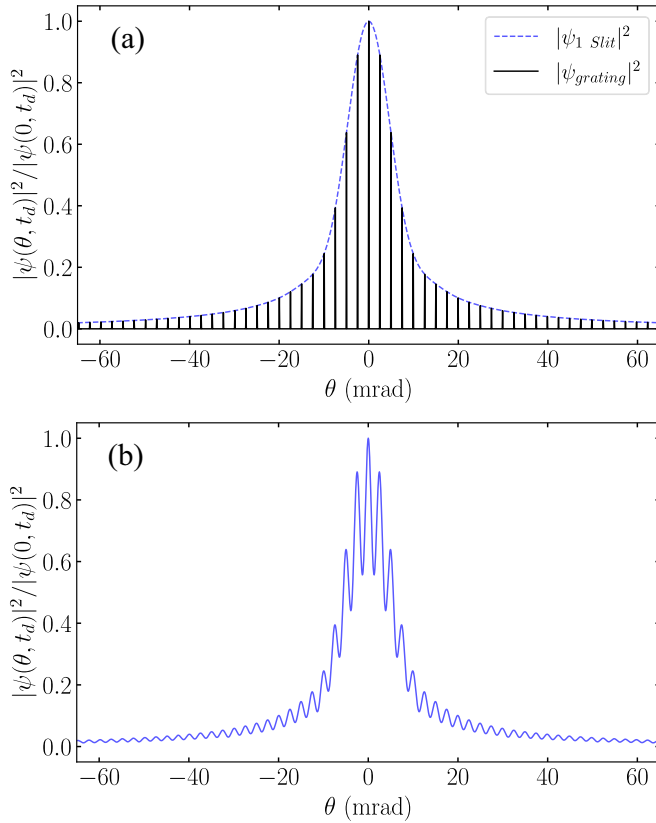


FIG. 4. (a) Square modulus of the wave function $|\psi(x, t_e + T)|^2$ at the detector for the diffraction by one slit $|\psi_{1slit}|^2$ (dashed-blue line) and by $N \gg 1$ slits $|\psi_{grating}|^2$ (solid-black line) as a function of the diffraction angle $\theta = \arctan(x/D_{GD}) \simeq x/D_{GD}$. Both functions are related to Eq. (7), where $|\psi_{1slit}|^2$ is the envelope for $|\psi_{grating}|^2$, in a similar way as in wave optics. (b) Example of the expected diffraction pattern of a N -slits nanograting obtained with our numerical simulations taking into account incoherence effects. The chosen angular beam divergence is $\sigma = 0.8$ mrad.

B. Probability density at the detector and incoherence effects

After an interaction time t_e with the grating, the wave function propagates freely to the detector for a time T . For the set of parameters chosen, the result is shown in Fig. 4 for the diffraction by one slit and by N -slits ($N \gg 1$). Moreover, when parameters such as R_{\min} (ranging from 0.25 to 1.2 nm) and l_{ab} (ranging from 5 to 25 nm) are varied, the diffraction picture on the detector remains largely unchanged, with a relative difference of less than 3×10^{-4} (see Appendix D). The insensitivity of the minimum potential position R_{\min} suggests that the surface corrugations resulting from the grating manufacturing process, which are on the level of 1 nm, have minimal impact on the diffraction pattern. In order to simulate a real experiment, incoherence effects must be taken into account. In general, the incoherence effects come from the spatial extension of the source, related to the van Cittert–Zernike theorem, and from the nonmonochromaticity of the atomic source, related to the Wiener–Khinchin theorem, leading to longitudinal k_z and transversal k_x momenta distributions. In general, both the spatial extension of the source and the transverse k_x momentum distribution can be well approx-

imated by a Gaussian function. Nevertheless, the longitudinal k_z distribution varies significantly from one experiment to another and is considered as an incoherent sum over all velocities. As a result, under these assumptions, we can describe the aforementioned incoherence effects by convolving the ideal case of the diffraction by N -slits $|\psi(\theta \simeq x/D_{GD}, t_e + T)|^2$ by a Gaussian distribution,

$$G(\theta) = \frac{1}{\sqrt{2\pi\sigma^2}} \exp\left(-\frac{\theta^2}{2\sigma^2}\right), \quad (13)$$

where $\theta = \arctan(x/D_{GD})$ is the diffraction angle and σ the standard deviation of the distribution. In a typical experiment, σ does not exceed 1 mrad, corresponding to a well-collimated beam. The final diffraction pattern is thus $I(\theta, t_e + T) = |\psi(\theta, t_e + T)|^2 * G(\theta)$ and is shown in Fig. 4 for an angular beam distribution of 0.8 mrad. The angular beam distribution being small, we verify that its influence on the wave packet propagation at normal incidence is negligible.

IV. COMPARISON WITH THE SEMICLASSICAL APPROACH

In this section, the numerical results obtained are compared with the commonly used semiclassical approach. For the comparison, we will only consider the diffraction by one slit [which is related to the N -slits diffraction by Eq. (5)] and we will not include the incoherence effects. The geometrical parameters of the nanogratings remain the same as in the previous sections, as well as the strength of the Casimir-Polder interaction parameter C_3 . In the semiclassical approach, the diffraction amplitude at the detector $\psi_{SC}(x, t_e + T)$ is described with classical waves, which can be developed through Kirchhoff's diffraction formula [34]

$$\psi_{SC}(x, t_e + T) \propto \int \left(\frac{\cos \mathcal{V} + \cos \mathcal{V}'}{2\lambda} \right) \psi_0(x', t_e) \times \exp\left(i \frac{2\pi x x'}{\lambda D_{GD}}\right) dx', \quad (14)$$

where $\psi_0(x', t_e)$ is atomic wave function at the output of the slit, $\mathcal{V} = \arctan(|x - x'|/D_{GD})$ and $\mathcal{V}' = \arctan(v'_x/v_z)$ are the geometric correction angles. This expression is valid in the Fresnel approximation, i.e., as long as the propagation distance D_{GD} satisfies the inequality $D_{GD} \gg a_s$. This condition is met in the simulations since we study the diffraction pattern in the far-field regime with a Fresnel number $\mathcal{F} \ll 10^{-3}$. In the framework of the semiclassical treatment of the atomic center of mass motion, referred as the time-dependent quasiclassical approximation, the atomic wave function is estimated by means of action integrals along classical trajectories [35]. In this approximation, the phase varies very rapidly along the different possible paths of the interferometer, and most of the interference will be destructive, except for the classical path. In this case, the wave function $\psi_0(x', t_e)$ writes

$$\psi_0(x', t_e) = \exp\left(\frac{i}{\hbar} S(x', t_e)\right), \quad (15)$$

where

$$S(x', t_e) = \int_0^{t_e} L(t) dt \quad (16)$$

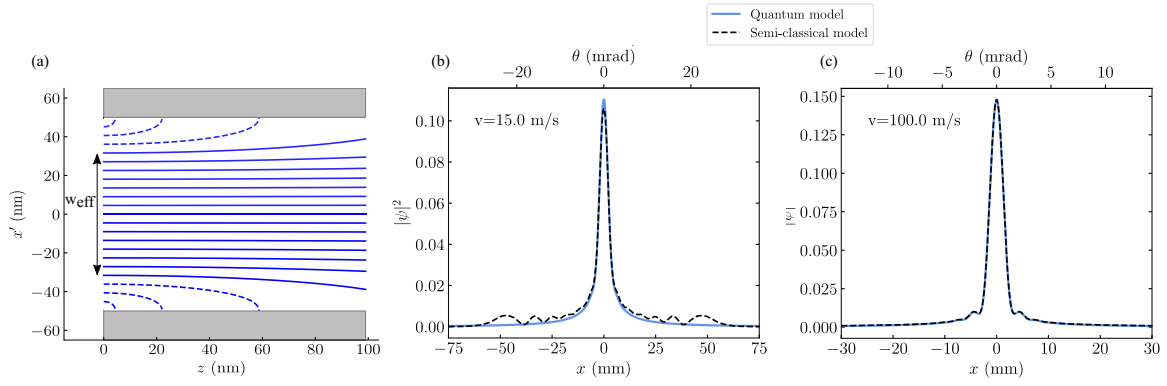


FIG. 5. Comparison between the single-slit diffraction pattern derived from the numerical simulation and the semiclassical model. The numerical simulations are performed with grating wall size $a_s = 100$ nm, grating thickness $l_G = 100$ nm, $C_3 = 5.04$ meV nm³ and a propagation time from the grating to the detector $T = 21$ ms. These parameters ensure that the far-field regime is reached. In (a), an example of classical particles motion governed by Newton's law $m\ddot{r} = -\nabla V_{vdW}$. The velocity of the incoming particles is set to $v = 15$ m/s. To include the absorption effect in the simulation, atoms reaching the coordinate $x' = \pm a_s/2 - r_{\min}$ during their propagations inside the slit are removed (dashed lines). This corresponds to an effective slit width W_{eff} [11]. The fraction F of atoms leaving the slits is thus given by $F = W_{\text{eff}}/a_s$. In (b) and (c) we compare the normalized diffraction pattern obtained by the semiclassical approach with the numerical simulation for atomic velocities of $v = 15$ m/s and $v = 100$ m/s. We find a good agreement for the high velocity $v = 100$ m/s. However, at the low velocity $v = 15$ m/s a significant disagreement is observed.

is the action integral along the classical trajectories. Developing Eq. (16) we have

$$\begin{aligned} \psi_0(x', t_e) = & \exp\left(\frac{i}{2\hbar} m v_z^2 t_e\right) \times \exp\left(\frac{im}{2\hbar} \int_0^{t_e} v_{x'}^2(t) dt\right) \\ & \times \exp\left(-\frac{i}{\hbar} V_{vdW}(x') t_e\right), \end{aligned} \quad (17)$$

where v_z (respectively $v_{x'}$) is the particle velocity in the z (respectively x') axis inside the slits. The first term, which is independent of x' , acts as a global phase and thus does not have a contribution to the diffraction pattern. The second term allows to go beyond the eikonal approximation, i.e., when the atomic trajectories are not constrained on the z axis. In fast atom beam experiments, with velocities between 200 m/s and 2000 m/s, this term is generally almost constant and is thus neglected in the phase estimation [9–11].

In Fig. 5, we compare the diffraction patterns obtained by the semiclassical approach and the quantum model. We observe that at high velocity ($v = 100$ m/s), the two figures are very similar. On the contrary, at low velocity ($v = 15$ m/s), the semiclassical approach fails to reproduce the numerical result. This observation is highlighted by plotting the following dimensionless quantity

$$A = \frac{\int_{-\infty}^{\infty} |\psi_{SC}(x)|^2 - |\psi(x)|^2 dx}{\int_{-\infty}^{\infty} |\psi(x)|^2 dx} \quad (18)$$

as the function of the velocity v of the incoming atoms. A quantifies the relative difference between the two models. The result is plotted in Fig. 6. Note that for $v \geq 50$ m/s, A remains small, meaning that both models give similar results. However, for $v \leq 50$ m/s, A increases rapidly as v decreases, indicating a significant discrepancy between the two models, especially in the tails of the distribution. To

explain such differences, we can check the validity conditions of the semiclassical approach at the exit of the slit ($t = t_e$), which are

$$\lambda \frac{\nabla V_{vdW}}{V_{vdW}} = \frac{3\lambda}{x \pm a_s/2} \ll 1 \quad (19a)$$

and

$$\frac{1}{2\pi} \left| \frac{d\lambda}{dx} \right| \ll 1. \quad (19b)$$

The first condition means that the de Broglie wavelength λ of the particle must be much shorter than the scale on which the potential V_{vdW} changes significantly. The second condition means that the spatial variation of the de Broglie wavelength must be small. For large velocities, both conditions are well met, except close to the surfaces of the slit. For example, at $v = 100$ m/s we have $\lambda(\nabla V_{vdW})/V_{vdW} = 0.15$ and $\frac{1}{2\pi} \left| \frac{d\lambda}{dx} \right| = 0.03$ at 2.7 nm from the surface. This explains why the quantity A saturates at a finite value for large velocities. This feature leads to a tiny difference in the tails of the quantum and semiclassical diffraction patterns. At low velocities, the conditions of Eq. (19) are not sufficiently satisfied to find a good agreement between the two models. For instance, at $v = 10$ m/s we find $\lambda(\nabla V_{vdW})/V_{vdW} = 0.36$ and $\frac{1}{2\pi} \left| \frac{d\lambda}{dx} \right| = 0.1$ at 6.5 nm from the surface. Moreover, this discrepancy at low velocity is certainly increased by the possibility that trajectories other than the classical ones might play a role in the action integral $S(x', t_e)$ [36].

In addition to the diffraction pattern, the fraction F of atoms exiting the slit can be studied and compared for the two models. For the semiclassical models, atoms reaching the position $x' = \pm a_s/2 - r_{\min}$ are considered lost, resulting in an effective slit size W_{eff} [see Fig. 5(a)]. The fraction F can thus be expressed as $F = W_{\text{eff}}/a_s$. In the quantum model, the norm of the wave packet $\psi(x, t)$ is computed to extract

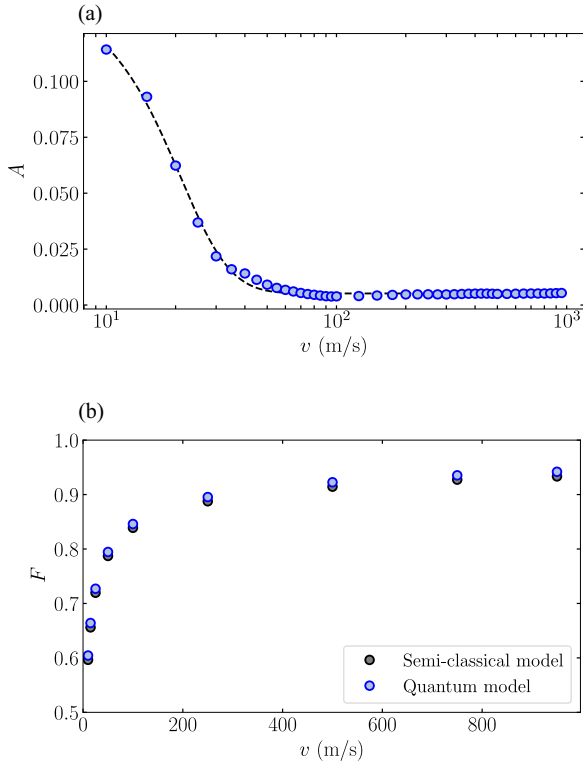


FIG. 6. (a) Dimensionless quantity A as a function of the velocity v of the incoming atoms. A quantifies the relative difference between the normalized semiclassical $|\psi_{SC}(x)|^2$ wave function and the quantum $|\psi(x)|^2$ wave function. The black-dashed line is a fit that serves as a guide for the eye. We observe that A decreases for large velocities, i.e., the higher the velocity the closer the two models are. Below $v = 50$ m/s, A increases rapidly as v decreases, suggesting a threshold in the validity of the semiclassical model with the parameters considered. (b) Fraction F of atoms exiting the slit as a function of the velocity v . Remarkably, almost identical results are obtained for both models.

the atom losses. The result for the two models is plotted in Fig. 6. Interestingly, we observe that both models give similar results, the difference being at the percent level, with the quantum model giving a slightly higher fraction F . We also find that, as expected, the lower the atom velocity, the lower the fraction F , meaning that more and more atoms are lost during the propagation inside the slits. This result strengthens our confidence in the validity of the comparison we have made between the two models.

To conclude, Fig. 6 shows that the two models give similar results in terms of the fraction of atoms lost. However, in terms of the diffraction pattern (i.e., when atoms are not lost during the propagation), at low velocities and in the tails of the distributions, the semiclassical approach fails and a quantum simulation must be performed.

V. CONCLUSIONS

In this paper, we have presented quantum numerical simulations of atomic diffraction by materials nanogratings. Our simulations are based on a numerically efficient solution of the time-dependent Schrödinger equation. After describing

the method and model used, we have demonstrated that our approach goes beyond the semiclassical approach used so far. In particular, we show that our model is able to describe interferometers with low atomic velocities and to capture near-surface effects.

This quantum model could thus be exploited in future experiments with slow atomic or molecular beams. For example, the consequences of long-range quantum reflection [37] (i.e., tens of nanometers away from the surface, where no absorption takes place) could be explored. In addition, the increased precision may allow the study of short-range repulsive interactions, which are difficult to describe theoretically with accuracy. This could be done by comparing experiments and numerical simulations based on the present quantum model, where imperfections of the nanogratings such as geometrical parameter dispersions or exact slit shape can be easily implemented. Finally, this model going beyond the semiclassical approach is also relevant to search for possible deviations from Newtonian gravity that could occur at the submicron scale [38].

ACKNOWLEDGMENTS

We wish to acknowledge Johannes Fiedler for fruitful discussions. This work has been supported by Region Ile-de-France in the framework of DIM SIRTEQ and partially supported by structure fédérative de recherche NAP MOSAIC of the University Sorbonne Paris Nord. N.G. acknowledges funding from the Deutsche Forschungsgemeinschaft (German Research Foundation) under Germany's Excellence Strategy (EXC-2123 QuantumFrontiers Grants No. 390837967) and through CRC 1227 (DQ-mat) within Projects No. A05, and the German Space Agency at the German Aerospace Center (Deutsche Raumfahrtagentur im Deutschen Zentrum für Luft- und Raumfahrt, DLR) with funds provided by the German Federal Ministry of Economic Affairs and Climate Action due to an enactment of the German Bundestag under Grants No. 50WM2250A and No. 50WM2250E (QUANTUS+) and No. 50WM2253A (AI-Quadrat).

APPENDIX A: STATIONARY PHASE APPROXIMATION

After a propagation time t_e inside the slit, the wave function $\psi(x, t_e)$ evolves freely for a time T . Therefore, the wave function at $t_f = t_e + T$ is

$$\psi(x, t_f) = \frac{1}{\sqrt{2\pi}} \int_{-\infty}^{+\infty} e^{-i\frac{\hbar k^2}{2m}T} \tilde{\psi}(k, t_e) e^{ikx} dk. \quad (\text{A1})$$

The global phase is stationary for

$$k = k_s = \frac{mx}{\hbar T}. \quad (\text{A2})$$

With a second-order Taylor expansion at $k = k_s$, we have

$$\begin{aligned} \tilde{\psi}(k, t_e) &\simeq \tilde{\psi}(k_s, t_e) + (k - k_s) \tilde{\psi}'(k_s, t_e) \\ &\quad + \frac{(k - k_s)^2}{2} \tilde{\psi}''(k_s, t_e) \end{aligned} \quad (\text{A3})$$

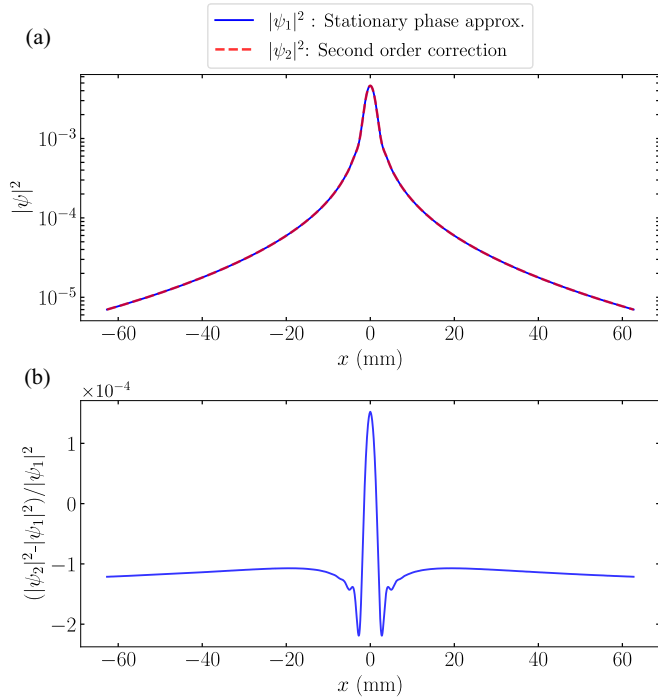


FIG. 7. (a) Probability density $|\psi(x, t_f)|^2$ in the stationary phase approximation ($|\psi_1|^2$, blue-solid line) and with the second-order correction ($|\psi_2|^2$, red-dashed line). For the simulations, the initial velocity is set to $v = 15$ m/s and the slit geometry is the following: $a_s = 100$ nm and $l_G = 100$ nm. The strength of the Casimir-Polder interaction is fixed at $C_3 = 5.04$ meV nm³ and the wave function freely expands during $T = 21$ ms. (b) Relative error between $|\psi_1|^2$ and $|\psi_2|^2$. We observe that the maximum relative error is around 2×10^{-4} , showing that the stationary phase approximation is an excellent approximation here.

and Eq. (A1) writes

$$\begin{aligned} \psi(x, t_f) \simeq & \frac{\tilde{\psi}(k_s, t_e)}{\sqrt{2\pi}} \int_{-\infty}^{+\infty} e^{-i\frac{\hbar k^2}{2m}T} e^{ikx} dk \\ & + \frac{\tilde{\psi}'(k_s, t_e)}{\sqrt{2\pi}} \int_{-\infty}^{+\infty} (k - k_s) e^{-i\frac{\hbar k^2}{2m}T} e^{ikx} dk \\ & + \frac{\tilde{\psi}''(k_s, t_e)}{2\sqrt{2\pi}} \int_{-\infty}^{+\infty} (k - k_s)^2 e^{-i\frac{\hbar k^2}{2m}T} e^{ikx} dk. \end{aligned} \quad (\text{A4})$$

This expression finally yields

$$\psi(x, t_f) \simeq \sqrt{\frac{m}{\hbar T}} e^{i(\frac{mx^2}{2\hbar T} - \frac{\pi}{4})} \left[\tilde{\psi}(k_s, t_e) - i \left(\frac{m}{2\hbar T} \right) \tilde{\psi}''(k_s, t_e) \right]. \quad (\text{A5})$$

The first term in Eq. (A5) corresponds to the so-called stationary phase approximation, and the second term is the first nonzero correction to this approximation. It is by nature a second-order term. To quantify the validity of the stationary phase approximation, we plot in Fig. 7 the probability density $|\psi(x, t_f)|^2$ without and with this second-order correction. We observe negligible differences between the two functions, the error bound being below 2×10^{-4} . In conclusion, the stationary phase approximation yields negligible error and can be used safely in our development.

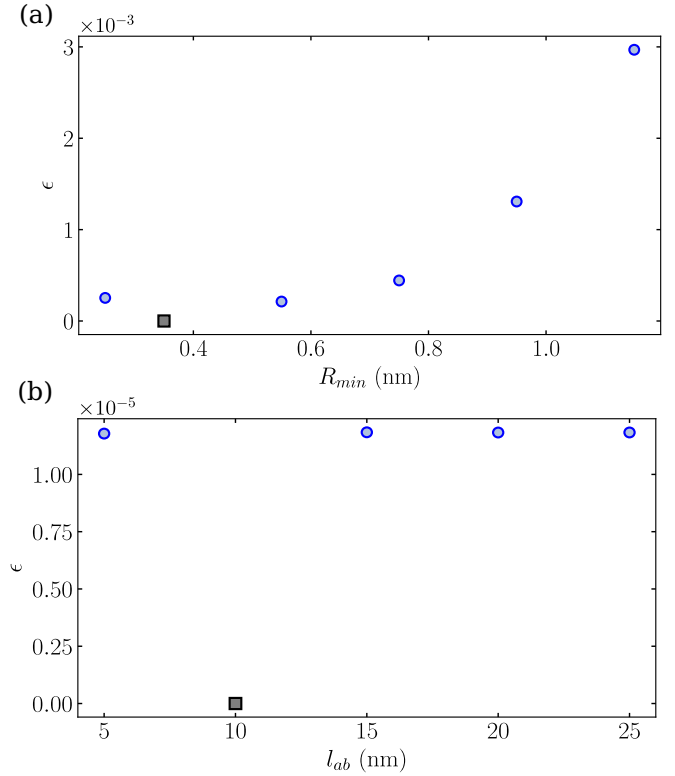


FIG. 8. Maximum relative difference ϵ between the probability density $|\psi_{\text{ref}}(x)|^2$ computed with the standard values $R_{\min} = 0.35$ nm and $l_{ab} = 5$ nm, and the probability density $|\psi(x)|^2$ for different values of R_{\min} and l_{ab} . In (a), the value of R_{\min} is varied, while in (b), the length l_{ab} is changed. The black square point denotes $|\psi_{\text{ref}}(x)|^2 = |\psi(x)|^2$.

APPENDIX B: ESTIMATION OF THE MINIMUM ATOM-SURFACE DISTANCE

Throughout the paper we consider argon (Ar) atoms in the metastable 3P_2 state interacting with a Si_3N_4 nanograting. For numerical applications and simulations, the minimum atom-surface distance r_{\min} must be evaluated. We assume that Ar atoms have a spherical electronic configuration with radius R and that $r_{\min} = R$. Using Bohr's model, the energy is given in eV by

$$E \simeq -13.6 \left(\frac{Z^*}{n^*} \right)^2, \quad (\text{B1})$$

while the radius of the atom is given in atomic units by

$$R \simeq \frac{(n^*)^2}{Z^*}, \quad (\text{B2})$$

where n^* is the effective quantum number and Z^* the effective nuclear charge. For Ar atoms in the 3P_2 state, Slater's rules give $n^* = 3.7$ and $Z^* = 2.05$. The numerical application leads to $E = -11.59$ eV for the state 3P_2 , close to the measured value $E = -11.55$ eV [39]. This confirms the hypothesis of spherical electronic configuration for Ar. For the radius we find $R = r_{\min} = 0.35$ nm, which is the value used throughout the paper.

APPENDIX C: 9-3 REPULSIVE LENNARD-JONES POTENTIAL

For each wall of the slits, the short-range repulsive potential due to the Pauli repulsion is modeled with the repulsive part of the Lennard-Jones potential assuming pairwise interactions. This approximation assumes that the interaction of an atom with the surface is proportional to the sum of the interactions with each of the atoms composing the surface. Multibody interactions are thus neglected. Using a Lennard-Jones interaction between atoms that scales as $1/x^{12}$, the pairwise model can be expressed as follows:

$$V_{LJ}(x) = - \int_V d^3r' \frac{\rho C_{12}}{|r - r'|^{12}}, \quad (C1)$$

where ρ is the atomic density of the surface (which is assumed to be constant) and C_{12} is the atom-atom repulsive interaction constant. Assuming that the surface grating can be treated as an infinitely extended plane, the potential for the walls of the slits located at $x = \pm a_s/2$ is written as

$$\begin{aligned} V_{LJ}(x) &= \int_0^{2\pi} \int_0^\infty \int_0^\infty \frac{C_6 \rho r' d\theta dr' dx'}{[(x \pm a_s/2 - x')^2 + r'^2]^6} \\ &= \frac{\pi}{50} \frac{C_6 \rho}{(a_s/2 \pm x)^9}. \end{aligned} \quad (C2)$$

Identifying $C_{\text{rep}} = \frac{\pi}{50} C_6 \rho$, this potential is the one implemented in Eq. (9), used for to represent the repulsive part of the total potential.

APPENDIX D: R_{\min} AND l_{ab} IMPACT ON THE ONE-SLIT DIFFRACTION PATTERN

To investigate the influence of parameters such as R_{\min} and l_{ab} on the diffraction pattern, we analyze the one-slit probability density on the detector at time $t = t_f$. Specifically, we vary R_{\min} from 0.25 to 1.2 nm and l_{ab} from 5 to 25 nm. In Fig. 8, we plot the maximum relative difference ϵ between the probability density $|\psi_{\text{ref}}(x)|^2$ using the standard values $R_{\min} = 0.35$ nm and $l_{ab} = 5$ nm and the probability density $|\psi(x)|^2$ for different values of R_{\min} and l_{ab} ,

$$\epsilon = \text{Max} \left| \frac{|\psi_{\text{ref}}(x)|^2 - |\psi(x)|^2}{|\psi_{\text{ref}}(x)|^2} \right|. \quad (D1)$$

We observe small values of ϵ , demonstrating the negligible influence of R_{\min} and l_{ab} on the diffraction pattern.

[1] R. Geiger, A. Landragin, S. Merlet, and F. Pereira Dos Santos, High-accuracy inertial measurements with cold-atom sensors, *AVS Quantum Sci.* **2**, 024702 (2020).

[2] S. Machluf, Y. Japha, and R. Folman, Coherent Stern–Gerlach momentum splitting on an atom chip, *Nat. Commun.* **4**, 2424 (2013).

[3] A. D. Cronin, J. Schmiedmayer, and D. E. Pritchard, Optics and interferometry with atoms and molecules, *Rev. Mod. Phys.* **81**, 1051 (2009).

[4] G. M. Tino, Testing gravity with cold atom interferometry: results and prospects, *Quantum Sci. Technol.* **6**, 024014 (2021).

[5] I. Dutta, D. Savoie, B. Fang, B. Venon, C. L. Garrido Alzar, R. Geiger, and A. Landragin, Continuous cold-atom inertial sensor with 1 nrad/sec rotation stability, *Phys. Rev. Lett.* **116**, 183003 (2016).

[6] S. Y. Buhmann, *Dispersion Forces I: Macroscopic Quantum Electrodynamics and Ground-State Casimir, Casimir–Polder and van der Waals Forces* (Springer, Heidelberg, 2012).

[7] L. W. Bruch, M. W. Cole, and E. Zaremba, *Physical Adsorption: Forces and Phenomena* (Clarendon, Oxford, 1997).

[8] J. Fiedler and B. Holst, An atom passing through a hole in a dielectric membrane: Impact of dispersion forces on mask-based matter-wave lithography, *J. Phys. B: At. Mol. Opt. Phys.* **55**, 025401 (2022).

[9] J. D. Perreault, A. D. Cronin, and T. A. Savas, Using atomic diffraction of Na from material gratings to measure atom-surface interactions, *Phys. Rev. A* **71**, 053612 (2005).

[10] S. Lepoutre, H. Jelassi, V. P. A. Lonij, G. Tréneç, M. Büchne, A. D. Cronin, and J. Vigué, Dispersive atom interferometry phase shifts due to atom-surface interactions, *Europhys. Lett.* **88**, 20002 (2009).

[11] R. E. Grisenti, W. Schöllkopf, J. P. Toennies, G. C. Hegerfeldt, and T. Köhler, Determination of atom-surface van der Waals potentials from transmission-grating diffraction intensities, *Phys. Rev. Lett.* **83**, 1755 (1999).

[12] R. Brühl, P. Fouquet, R. E. Grisenti, J. P. Toennies, G. C. Hegerfeldt, T. Köhler, M. Stoll, and C. Walter, The van der Waals potential between metastable atoms and solid surfaces: Novel diffraction experiments vs theory, *Europhys. Lett.* **59**, 357 (2002).

[13] C. Brand, M. Sclafani, C. Knobloch, Y. Lilach, T. Juffmann, J. Kotakoski, C. Mangler, A. Winter, A. Turchanin, J. Meyer *et al.*, An atomically thin matter-wave beamsplitter, *Nat. Nanotechnol.* **10**, 845 (2015).

[14] C. Garcion, N. Fabre, H. Bricha, F. Perales, S. Scheel, M. Ducloy, and G. Dutier, Intermediate-range Casimir-Polder interaction probed by high-order slow atom diffraction, *Phys. Rev. Lett.* **127**, 170402 (2021).

[15] M. D. Gregoire, I. Hromada, W. F. Holmgren, R. Trubko, A. D. Cronin, Measurements of the ground-state polarizabilities of Cs, Rb, and K using atom interferometry, *Phys. Rev. A* **92**, 052513 (2015).

[16] L. Hackermüller, K. Hornberger, S. Gerlich, M. Gring, H. Ulbricht, and M. Arndt, Optical polarizabilities of large molecules measured in near-field interferometry, *Appl. Phys. B* **89**, 469 (2007).

[17] R. Trubko, J. Greenberg, M. T. St. Germaine, M. D. Gregoire, W. F. Holmgren, I. Hromada, and A. D. Cronin, Atom interferometer gyroscope with spin-dependent phase shifts induced by light near a tune-out wavelength, *Phys. Rev. Lett.* **114**, 140404 (2015).

[18] A. D. Cronin and J. D. Perreault, Phasor analysis of atom diffraction from a rotated material grating, *Phys. Rev. A* **70**, 043607 (2004).

- [19] S. Nimmrichter and K. Hornberger, Theory of near-field matter-wave interference beyond the eikonal approximation, *Phys. Rev. A* **78**, 023612 (2008).
- [20] B. Herwerth, M. DeKieviet, J. Madroñero, and S. Wimberger, Quantum reflection from an oscillating surface, *J. Phys. B: At. Mol. Opt. Phys.* **46**, 141002 (2013).
- [21] E. Galiffi, C. Sünderhauf, M. DeKieviet, and S. Wimberger, Two-dimensional simulation of quantum reflection, *J. Phys. B: At. Mol. Opt. Phys.* **50**, 095001 (2017).
- [22] The plane wave character of the incoming atoms is justified by the large size of the atomic wave-packet reaching the nanostructure after expanding freely from the source, exceeding by several orders of magnitude the typical slit size a_s .
- [23] L. Mandel and E. Wolf, *Optical Coherence and Quantum Optics* (Cambridge University Press, Cambridge, 1995).
- [24] J. M. Wylie and J. E. Sipe, Quantum electrodynamics near an interface, *Phys. Rev. A* **30**, 1185 (1984).
- [25] J. M. Wylie and J. E. Sipe, Quantum electrodynamics near an interface. II, *Phys. Rev. A* **32**, 2030 (1985).
- [26] The value of the C_3 coefficient is calculated in the framework of Lifshitz theory, assuming a semi-infinite plan and inferring the spectral response of the Si_3N_4 material through the two following references: H. R. Philipp, Optical properties of silicon nitride, *J. Electrochem. Soc.* **120**, 295 (1973); K. Luke, Y. Okawachi, M. R. E. Lamont, A. L. Gaeta, and M. Lipson, Broadband mid-infrared frequency comb generation in a Si_3N_4 microresonator, *Opt. Lett.* **40**, 4823 (2015).
- [27] P. Bryk, S. Sokolowski, and D. Henderson, Some aspects of the adsorption of a Lennard-Jones gas on a rough surface, *J. Chem. Phys.* **110**, 15 (1999).
- [28] A. Maury, M. Donaire, M. P. Gorza, A. Lambrecht, and R. Guérout, Surface-modified Wannier-Stark states in a one-dimensional optical lattice, *Phys. Rev. A* **94**, 053602 (2016).
- [29] V. P. A. Lonij, W. F. Holmgren, and A. D. Cronin, Magic ratio of window width to grating period for van der Waals potential measurements using material gratings, *Phys. Rev. A* **80**, 062904 (2009).
- [30] W. Vassen, C. Cohen-Tannoudji, M. Leduc, D. Boiron, C. I. Westbrook, A. Truscott, K. Baldwin, G. Birkl, P. Cancio, and M. Trippenbach, Cold and trapped metastable noble gases, *Rev. Mod. Phys.* **84**, 175 (2012).
- [31] R. Kosloff and D. Kosloff, Absorbing boundaries for wave propagation problems, *J. Comput. Phys.* **63**, 363 (1986).
- [32] A. N. Hussain and G. Roberts, Procedure for absorbing time-dependent wave functions at low kinetic energies and large bandwidths, *Phys. Rev. A* **63**, 012703 (2000).
- [33] M.D. Feit, J. A. Fleck, and A. Steiger, Solution of the Schrödinger equation by a spectral method, *J. Comput. Phys.* **47**, 412 (1982).
- [34] M. Born and E. Wolf, *Principles of Optics: Electromagnetic Theory of Propagation, Interference and Diffraction of Light*, 7th ed. (Cambridge University Press, Cambridge, 1999).
- [35] C. Henkel, J.-Y. Courtois, and A. Aspect, Atomic diffraction by a thin phase grating, *J. Phys. II France* **4**, 1955 (1994).
- [36] S. Garashchuk and D. Tannor, Calculation of autocorrelation functions using the Wigner representation of quantum mechanics, *Chem. Phys. Lett.* **263**, 324 (1996).
- [37] B. S. Zhao, Z. Zhang, and W. Schöllkopf, Universal diffraction of atoms and molecules from a quantum reflection grating, *Sci. Adv.* **2**, e1500901 (2016).
- [38] G. L. Klimchitskaya, P. Kuusk, and V. M. Mostepanenko, Constraints on non-Newtonian gravity and axionlike particles from measuring the Casimir force in nanometer separation range, *Phys. Rev. D* **101**, 056013 (2020).
- [39] W. L. Wiese, J. W. Brault, K. Danzmann, V. Helbig, and M. Kock, Unified set of atomic transition probabilities for neutral argon, *Phys. Rev. A* **39**, 2461 (1989).